NANOROBOTS

Intracellular manipulation and measurement with multipole magnetic tweezers

X. Wang[1,2], C. Ho[1], Y. Tsatskis[3], J. Law[1], Z. Zhang[1], M. Zhu[1,4], C. Dai[1], F. Wang[5], M. Tan[6], S. Hopyan[4,7], H. McNeill[3,8], Y. Sun[1,2,9]*

Copyright © 2019 The Authors, some rights reserved; exclusive licensee American Association for the Advancement of Science. No claim to original U.S. Government Works

The capability to directly interrogate intracellular structures inside a single cell for measurement and manipulation is important for understanding subcellular and suborganelle activities, diagnosing diseases, and developing new therapeutic approaches. Compared with measurements of single cells, physical measurement and manipulation of subcellular structures and organelles remain underexplored. To improve intracellular physical measurement and manipulation, we have developed a multipole magnetic tweezers system for micromanipulation involving submicrometer position control and piconewton force control of a submicrometer magnetic bead inside a single cell for measurement in different locations (spatial) and different time points (temporal). The bead was three-dimensionally positioned in the cell using a generalized predictive controller that addresses the control challenge caused by the low bandwidth of visual feedback from high-resolution confocal imaging. The average positioning error was quantified to be 0.4 μm, slightly larger than the Brownian motion–imposed constraint (0.31 μm). The system is also capable of applying a force up to 60 pN with a resolution of 4 pN for a period of time longer than 30 min. The measurement results revealed that significantly higher stiffness exists in the nucleus' major axis than in the minor axis. This stiffness polarity is likely attributed to the aligned actin filament. We also showed that the nucleus stiffens upon the application of an intracellularly applied force, which can be attributed to the response of structural protein lamin A/C and the intracellular stress fiber actin filaments.

INTRODUCTION

Intracellular manipulation and measurement reveal the properties and functions of structures and organelles inside a cell (*1*). For instance, mechanical properties of the cell nucleus are directly linked to cardiac disease (*2*) and cancer (*3*), the properties and organization of the cytoskeleton regulate cell migration and mitosis (*4*), and the properties of endoplasmic reticulum (ER) control intracellular calcium storage and regulation (*5*). Understanding subcellular and suborganelle activities, diagnosing diseases, and developing potential therapeutic approaches demand the ability to directly interrogate intracellular structures inside a cell. Compared with measurements of single cells, physical measurement and manipulation of subcellular structures and organelles remain underexplored.

Techniques for intracellular manipulation and measurement can be classified into tethered and untethered approaches. Tethered techniques, such as the use of a sharp micropipette (*6*) and atomic force microscope (AFM) tip (*3*), are not suitable for long-term measurement inside a cell or for performing measurements at multiple locations on an intracellular structure, because tethered tools must maintain a hardware connection between the inside and the outside of the cell. Among untethered techniques, optical tweezers (*7*) have a low force output (less than 10 pN), and increasing laser power for larger force output (e.g., as required for deforming the cell nucleus) can cause damage to the intracellular structures. Intracellular navigation was demonstrated using acoustic tweezers to actuate gold nanorods (*8*). Open-loop control resulted in poor positioning accuracy, and the demonstration of intracellular positioning of a nanorod was limited to two dimensionals. Only low forces below 1 pN were generated on a nanorod of 3 μm in length and 300 nm in diameter. This level of force is insufficient for performing mechanical measurements on intracellular organelles. Further, increasing ultrasound power could agitate the medium environment both inside and outside the cell and may induce oxidative stress in the cells to manipulate (*9*).

Magnetic micromanipulation has recently undergone significant advances and has been applied to drug delivery (*10*), assembly of tissue constructs (*11*), and mechanical measurements (*12*) on the scale of millimeters to micrometers for applications at the organ (*13*), tissue (*14*), and cell (*15*) levels. As illustrated in Fig. 1A, a millimeter-scale device was controlled to move inside the stomach (tens of centimeters) for less-invasive imaging and biopsy (*14*); the OctoMag system navigated a submillimeter device inside the eye (several centimeters) for surgery (*13*); microswimmers were positioned inside the blood vessel (several millimeters) to mechanically clear blood clogs (*16*, *17*); and a 5-μm magnetic bead was navigated within a mouse embryo (~100 μm in diameter) for mechanical measurements on the inner cell mass (*18*). Magnetic helical swimmers (termed nanomotors) were demonstrated to navigate inside a cell (*9*). The helical swimmers' motion was shown to be sensitive to the local viscosity of the cytoplasm. These helical swimmers were not capable of performing mechanical measurement inside a cell because of low force generation. According to (*19*), to generate a large enough force (e.g., 50 pN) for mechanical measurement of intracellular organelles, a helical tail as long as 50 μm is needed. To advance magnetic micromanipulation further for realizing the "fantastic voyage" inside a single cell and perform mechanical measurements on intracellular organelles, a submicrometer magnetic bead must be introduced into the cell, three-dimensionally positioned

[1]Department of Mechanical and Industrial Engineering, University of Toronto, Toronto, Ontario M5S 3G8, Canada. [2]Institute of Biomaterials and Biomedical Engineering, Toronto, Ontario M5S 3G9, Canada. [3]Lunenfeld-Tanenbaum Research Institute, Mt. Sinai Hospital, Toronto, Ontario M5G 1X5, Canada. [4]Program in Developmental and Stem Cell Biology, The Hospital for Sick Children, Toronto, Ontario M5G 1X8, Canada. [5]HRG Central Institute of Robotics, HIT Robot Group, Harbin, Heilongjiang 150001, China. [6]Institute of Automation, Chinese Academy of Sciences, Beijing 100190, China. [7]Division of Orthopaedic Surgery, Hospital for Sick Children and University of Toronto, Toronto, Ontario M5G 1X8, Canada. [8]Department of Developmental Biology, Washington University School of Medicine, St. Louis, MO 63108, USA. [9]Department of Electrical and Computer Engineering, University of Toronto, Toronto, Ontario M5S 3G4, Canada.
*Corresponding author. Email: sun@mie.utoronto.ca

Downloaded from https://www.science.org at The Hong Kong University of Science and Technology (Guangzhou) on May 26, 2026

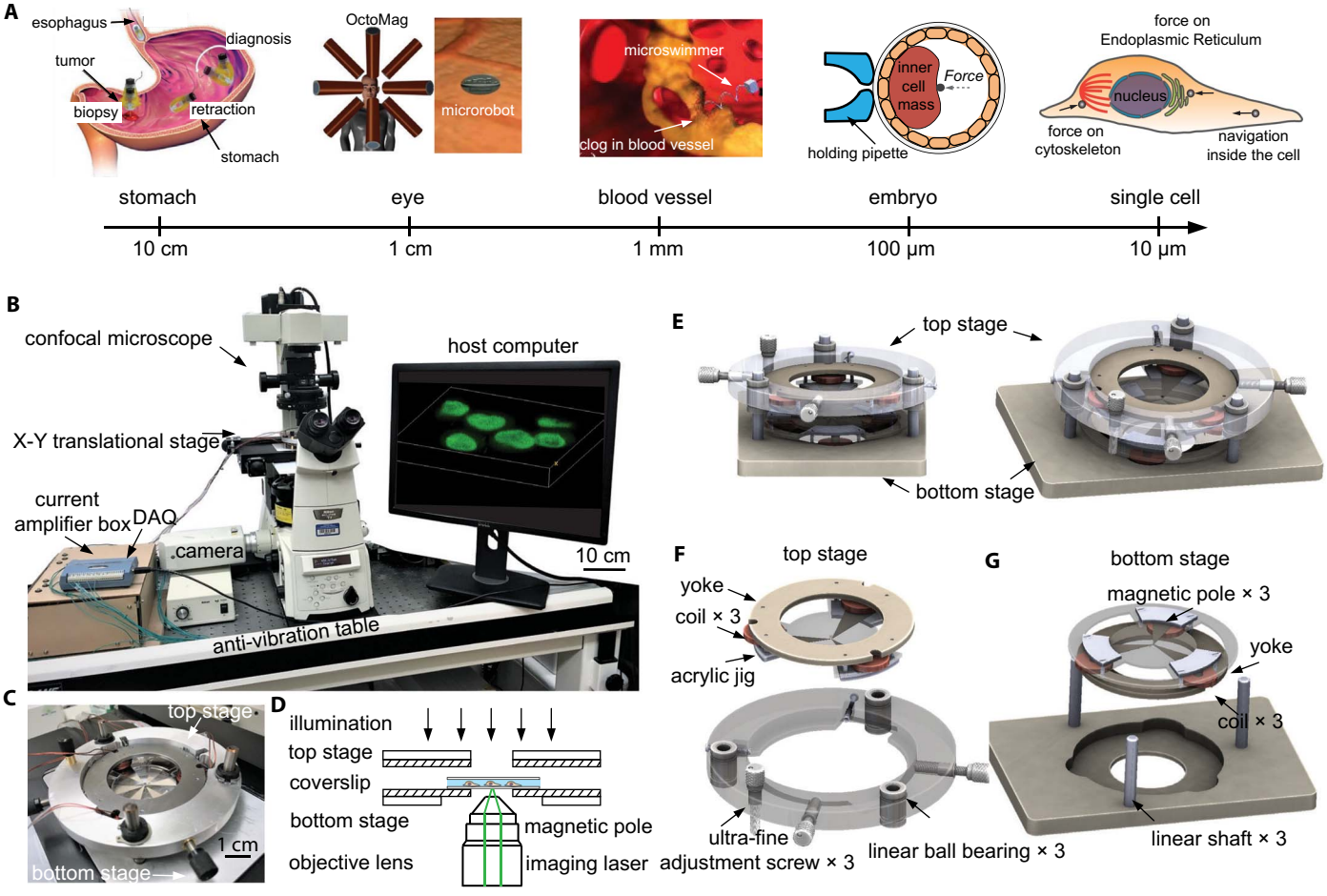

Fig. 1. Multipole magnetic tweezers system. (**A**) Applications of magnetic micromanipulation ranging from organ level (*13*, *14*), tissue level (*16*, *17*), to embryo level (*18*) and single-cell level. (**B**) The multipole magnetic tweezers was integrated with a confocal microscope. Figures were adapted from (*13*, *14*, *17*, *18*) with permissions. (**C**) Picture of the intracellular multipole magnetic tweezers integrated with the microscope stage. (**D**) Imaging light path and illumination light path. (**E**) Mechanical design of the multipole magnetic tweezers device. (**F**) Top stage includes yoke, three magnetic poles with three coils, and position control screws. (**G**) Bottom stage includes yoke, three magnetic poles with three coils, and structures for integration with confocal microscope.

to desired locations inside the cell without being limited by the heterogeneous cytoplasm, and accurately controlled to apply subnanonewton forces for intracellular measurements.

For intracellular manipulation and measurement, a magnetic bead can be introduced into the cell via microinjection or endocytosis. When magnetized, the bead can be navigated three-dimensionally inside the cell and controlled to apply forces onto intracellular structures. However, traditional single-pole magnetic tweezers are only capable of generating one-directional attractive force. In addition, traditional magnetic tweezers require magnetic beads to be attached on the surface of a sample. For example, a magnetic microbead was attached to the surface of an isolated cell nucleus and was vibrated for studying nucleus stiffening (*12*). For improved maneuvering of force directionality and bead positioning, a two-dimensional (2D) magnetic tweezers instrument was developed, where force could be exerted on a magnetic bead toward each of the three magnetic poles (*20*). To extend magnetic tweezers from 2D to 3D, a 3D multipole magnetic tweezers device was developed (*21*). For this device, when force directionality was controllable, the force output would be below 0.5 pN for a submicrometer magnetic bead. In addition, open-loop control of the device, as reported in (*21*), cannot achieve 3D position control and force control, preventing it from performing mechanical measurement on a specific intracellular structure.

To realize 3D intracellular manipulation and mechanical measurement, challenges in high-resolution imaging, submicrometer position control, and subnanonewton force control must be addressed. For instance, image feedback needs to be obtained from 3D imaging tools, such as a confocal microscope. The subcellular imaging resolution has a low feedback rate, posing difficulties in the dynamic control of a submicrometer bead. This limitation is exacerbated by the complex intracellular environment, such as the many filaments in the cytoplasm, making visual detection and tracking as well as control of the submicrometer bead difficult.

This paper presents a multipole magnetic tweezers system with unique capabilities. The multipole magnetic tweezers system was integrated onto a confocal microscope, enabling the control of a submicrometer magnetic bead inside a cell with high-resolution visual feedback. A generalized predictive control (GPC) algorithm was developed to account for bead dynamics and the low-bandwidth, high-resolution visual feedback. Visual tracking of the bead and intracellular structures with force control enabled bead navigation and intracellular measurement. The calibrated system was experimentally demonstrated

Downloaded from https://www.science.org at The Hong Kong University of Science and Technology (Guangzhou) on May 26, 2026

to be capable of 3D-positioning a 0.7-μm magnetic bead and applying forces up to 60 pN with a resolution of 4 pN. The magnetic bead was controlled to apply forces to different locations of the cell nuclear envelope. The measured force-deformation data revealed that the cell nucleus in the major axis is significantly stiffer than in the minor axis in human bladder cancer cells (T24). The quantified heterogeneity of nuclear mechanics showed the polarity of nuclear mechanics in intact cells. Enabled by the system's capability of temporal measurement, our experiments also deciphered that the cell nucleus stiffens under intracellular applied force in intact cells.

RESULTS

Design of a multipole magnetic system for intracellular navigation and measurement

Our multipole magnetic tweezers device consists of six magnetic poles with six coils (Fig. 1, B and E). Three coils and three poles were fabricated into the top stage; three coils and three poles were embedded into the bottom stage (Fig. 1, C and G). The multipole magnetic tweezers generated a large magnetic gradient by sharp pole tips (tip radius, <1.5 μm) made from high-permeability foil (Silicon Iron, MuShield). When current was applied to the coils, the magnetic beads (FCM-0856-2, Spherotech; bead size measured as 0.698 ± 0.007 μm for 20 beads imaged using a scanning electron microscope; permeability, 0.35 henries/m) in the workspace were magnetized and actuated. The design aimed to achieve 3D navigation of a submicrometer magnetic bead inside a cell and apply a force larger than 50 pN to deform the cell nucleus. The bead size was chosen to be 0.7 μm in diameter, considering the cell viability and success rate of introducing bead into the cell through endocytosis (shown in fig. S1). The target force was chosen as 50 pN, a force that is sufficient for deforming the cell nucleus.

According to the scaling law of magnetism, the magnetic gradient pulling force scales with volume and hence decreases by a power of three as the dimension of the target (i.e., bead) decreases in the magnetic gradient field. Meanwhile, magnetic gradient decays by a power of four with the distance between the magnetic pole and the bead to manipulate. The size of the magnetic bead was set to be in the submicrometer scale (0.7 μm in diameter) for easier introduction of the bead into a cell through endocytosis and for achieving a high cell viability (shown in fig. S1). To compensate for the scaling down of the magnetic force with the small bead size, we designed the distance between the magnetic pole tip and the manipulated magnetic bead to be small (150 μm) to use the scaling law for larger magnetic force while ensuring a large enough workspace for seeding and imaging cells. Compared with the multipole magnetic tweezers we previously developed for manipulation inside a mouse embryo (*18*) (bead size, 5 μm; maximum force, 120 pN), the distance between the pole and the bead was decreased from 400 to 150 μm in this new design. In addition to the distance between the pole tip and the bead to manipulate, driving current was designed to be 5 A, and coil turns set as 80 turns. The design parameters of the pole distance, currents, and coil turns (table S1) were simulated in ANSYS Maxwell before device construction, with field distribution and force map shown in Fig. 2 (A and D). The results showed that the maximum magnetic force exerted on a 0.7-μm magnetic bead is 66.2 pN within a workspace of 40 μm by 40 μm by 20 μm.

The close distance between poles required precise alignment and adjustment. For top and bottom stages, the poles were assembled onto an acrylic plate separately with alignment marks engraved by laser cutting. Following the alignment marks, poles on the same stage were positioned on the acrylic plate to ensure in-plane alignment accuracy. Then, the acrylic plates were mounted with yokes by jigs to form the integrated top and bottom magnetic circuits to strengthen the field. The jigs push magnetic poles against the yoke for close surface contact

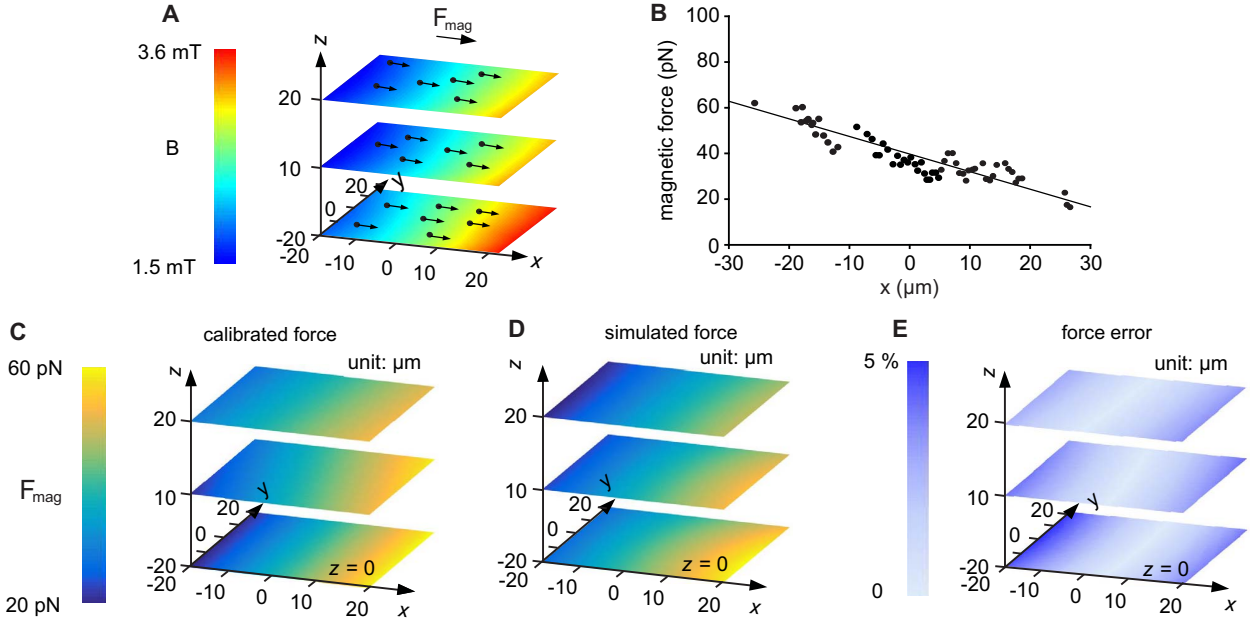

Fig. 2. Magnetic force simulation and calibration. (**A**) Multiple 0.7-μm beads were introduced into the workspace for force quantification in different positions. All beads moved toward the +*X* direction when a magnetic force was applied toward +*X*. (**B**) Calculated magnetic force in +*X* fitted into the magnetic force model (Eq. 1). The dots show the experimentally measured force, and the line shows the force model calculated force. (**C**) 3D magnetic field constructed by experimental results on different focal planes. (**D**) Finite element simulated magnetic force exerted on the bead. (**E**) Force error map in the workspace of 40 μm by 40 μm by 20 μm.

Downloaded from https://www.science.org at The Hong Kong University of Science and Technology (Guangzhou) on May 26, 2026

to reduce magnetic reluctance. Besides the alignment of the three poles on the top or bottom stage, the alignment of poles between top and bottom stages and the distance between the two stages must also be controlled and adjusted. The top stage contains two horizontal ultrafine adjustment screws for adjusting the top yoke and poles translationally in the *X*-*Y* plane to align the top layer poles with the bottom layer poles. By using the vertical ultrafine adjustment screw, the top stage can be moved up and down precisely, whereas three linear guides keep the top and bottom stages parallel to each other. The distance between the poles and stages was calibrated using a micromanipulator (MX7600, Siskiyou Inc.) with a positioning accuracy of 1 μm.

The device was integrated onto the stage of a standard confocal microscope (Fig. 1, B and C; Nikon C2 confocal microscope), which provides image feedback for bead position and force control. Cells were grown on a coverslip and put onto the sample holder between the top and bottom stages of the magnetic tweezers device. The laser-cut hole in the center of the bottom stage enables close contact between the coverslip and the objective lens (Fig. 1D). Laser only passes through the coverslip, ensuring high-quality imaging. The cell had a 0.7-μm magnetic bead introduced inside the cell, and the nucleus was fluorescently labeled (SYTO 9, Thermo Fisher Scientific).

Magnetic force modeling, bead dynamics, and force calibration

The magnetic field model reported in (*22*) related the normalized force, normalized current, and bead positions, enabling 3D position control. However, the model lacked a description of force quantification. We previously presented a model with force quantification and took into account the bead momentum change over time (*18*). However, when the size of the bead scales down below a micrometer, the momentum change (10^{-15} kg·m/s) of the bead becomes negligible because of the small mass compared with piconewton-level magnetic force and fluidic force. Thus,

$$\boldsymbol{F} = k_i {I_{\max}}^2 \nabla \hat{\boldsymbol{I}}^T \boldsymbol{N}_0 \hat{\boldsymbol{I}} + k_i {I_{\max}}^2 \begin{bmatrix} \frac{8}{l} & 0 & 0 \\ 0 & \frac{8}{l} & 0 \\ 0 & 0 & \frac{32}{l} \end{bmatrix} \begin{bmatrix} x \\ y \\ z \end{bmatrix} \quad (1)$$

where $\boldsymbol{F}$ is the generated magnetic force, k_i is a linear factor, $I_{\max}$ is the maximum driving current in the coils, $\hat{I}^T = \left[\frac{I_1}{I_{\max}} \quad \frac{I_2}{I_{\max}} \quad \frac{I_3}{I_{\max}} \quad \frac{I_4}{I_{\max}} \quad \frac{I_5}{I_{\max}} \quad \frac{I_6}{I_{\max}} \right]$, $\boldsymbol{N}_0$ is a six-by-six matrix reflecting the structure and magnetic reluctance of the device as derived in (*22*), and l is the distance from the hypothesized magnetic charge representing the poles and workspace center, which is further calibrated with k_i.

When the current is applied in the coils for bead actuation, the magnetic bead is subjected to a magnetic force, fluidic drag force, buoyancy, and gravity.

$$\boldsymbol{F} - 6\pi\eta r\boldsymbol{v} + \boldsymbol{F}_{\text{buoyance}} - \boldsymbol{G} = m\boldsymbol{a} \quad (2)$$

where η is the viscosity of the medium, $\boldsymbol{v}$ is the speed of the microbead, $6\pi\eta r\boldsymbol{v}$ is fluidic drag force, $\boldsymbol{F}_{\text{buoyance}}$ is buoyant force, $\boldsymbol{G}$ is gravity, and $\boldsymbol{a}$ is acceleration. The magnetic force and fluidic drag force are in the scale of 10^{-12} N, whereas gravity and buoyancy are in the scale of 10^{-14} N. In addition, because the mass of the bead is small (10^{-13} kg), the large acceleration (initially 10 m/s^2) increases velocity rapidly, increasing the fluidic drag force and resulting in the balance of magnetic force and fluidic drag force. Thus, Eq. 2 is rewritten into

$$k_i \nabla \boldsymbol{I}^T \boldsymbol{N}_0 \boldsymbol{I} + k_i {I_{\max}}^2 \boldsymbol{K}\boldsymbol{P} - 6\pi\eta r\dot{\boldsymbol{P}} = 0 \quad (3)$$

where $\boldsymbol{P} = [x \quad y \quad z]^T$ is the position of the bead in three dimensions and $\boldsymbol{K}$ is the three-by-three matrix shown in Eq. 1.

Experimentally, the generated magnetic force was calibrated through moving 0.7-μm beads in 200 mPa·s silicone oil (Brookfield). According to bead dynamics in Eq. 3, magnetic force was also quantified by calculating the balancing fluidic drag force. Multiple beads were introduced into the workspace. Input currents (2.6, −1.0, −0.6, −1.0, 0.6, and −0.6 A) generated a force of 40 pN in the workspace center along +*X* (Fig. 2A), according to the force model in Eq. 1. By measuring the velocity of each bead and calculating their fluidic drag force, the magnetic force on the beads was also quantified experimentally.

The magnetic force model (Eq. 1) shows that magnetic force depends on bead position and driving current in each coil. As shown in Fig. 2B, the linear factors k_i and l in Eq. 1 were experimentally calibrated by fitting the calculated magnetic force, driving currents, and bead positions. The same calibration procedure was repeated for the *Y* and *Z* directions. The calibration process was then repeated for different focal planes, resulting in a model-fitted experimental 3D magnetic force field (Fig. 2C).

Magnetic field generated in the workspace was also simulated in ANSYS Maxwell. Using the structure and magnetic properties (permeability and reluctance) of the device and inputting the same driving currents as used in experiments, we calculated in simulation magnetic force exerted on a 0.7-μm magnetic bead. Figure 2D shows the simulated magnetic force field on the same three planes as in experimental calibration. Subtraction between simulation-calculated force values and model-fitted experimental force values (Fig. 2E) is the force quantification error due to the nonlinearity of the magnetic field. Within the workspace of 40 μm by 40 μm by 20 μm, the error is within 5% of the simulated force value. The bead size variance and the nonlinearity of the field account for the 5% error in Fig. 2E. Force calibration confirmed that the system was capable of generating a maximum force of 60 pN with a resolution of 4 pN. The force resolution was quantified by the root mean square deviation between experimentally measured force (dots in Fig. 2B) and model-fitted force (fitted line in Fig. 2B).

Position control of the submicrometer magnetic bead

The bead position is controlled through controlling the driving currents in the coils, based on visual feedback from the confocal microscope. Brownian motion poses difficulties to the position control of a submicrometer bead. It was measured in phosphate-buffered saline that, for a 0.7-μm bead, the average mean square deviation between two successive images was 0.31 ± 0.07 μm (n = 5 beads) without magnetic force applied, indicating that the theoretically smallest positioning error to be about 0.31 μm for a 0.7-μm bead. Considering the random thermal force that induces Brownian motion, bead dynamics in Eq. 3 is rewritten as

$$\boldsymbol{F}_{\text{mag}} - \boldsymbol{F}_{\text{thermal}} = m\ddot{\boldsymbol{P}} + 6\pi\eta r\dot{\boldsymbol{P}} \quad (4)$$

where $\boldsymbol{F}_{\text{thermal}}$ is the random thermal force depending on bead size and environmental temperature. On the basis of the fluid drag force

Downloaded from https://www.science.org at The Hong Kong University of Science and Technology (Guangzhou) on May 26, 2026

during Brownian motion tracking for 5 min, its magnitude was experimentally quantified to be about 3 pN. $m\ddot{\boldsymbol{P}}$ is the inertia of the bead, which is negligible because of the bead's small mass. The scaling down of bead size causes bead mass to scale down by a factor of three. The small mass leads to small inertia. Thus, small force disturbance induces large deviations in bead position, based on Eq. 4. To overcome the force disturbance from the thermal force, the bead position control constraint that must be imposed to overcome the random thermal force is

$$|\boldsymbol{F}_{\text{mag}}| > \text{mean}(|\boldsymbol{F}_{\text{thermal}}|) + 3\sigma \quad (5)$$

Considering the limit of the device's force output of 60 pN, force constraint was set as [6 pN, 60 pN], based on which controller output constraint (current) was calculated using Eq. 1.

In addition, visual servoing alone [or proportional-integral-derivative (PID) controller alone] using the low visual feedback rate (1 to 4 frames/s) of laser scanning confocal microscopes cannot achieve position control with errors less than the diameter of the submicrometer bead, because the large sampling time leads to large overshoot and longer settling time (detailed in the Supplementary Materials). To address the challenges posed by the large sampling time, we used GPC for bead position control, which predicted bead positions between two successive frames of images (fig. S2). GPC used the bead dynamics described in Eq. 4, as well as bead position and velocity from the previous frame of image, to predict bead position and velocity for N times within one sampling period T_c. Compared with other model-based predictive control methods, GPC provides analytical solutions with weighting of control increments in the cost function (*23*, *24*), making it suitable for controlling our system that has low inertia and long sampling time.

With the control constraint for magnetic force (Eq. 5; large enough to dominate thermal force while smaller than maximum force generated by the system) during bead navigation, current output was calculated by the GPC controller to control the bead position (eq. S7). Experimental step responses showed that GPC had a smaller overshoot (0.75 μm versus 1.27 μm) and shorter settling time (1.1 s versus 4.3 s) than PID. The waypoint trajectory tracking of the 0.7-μm magnetic bead revealed an average deviation of 0.43 μm from the trajectory in cell medium (fig. S3 and table S2), which is smaller than the diameter of the magnetic bead.

Intracellular spatial measurement of nuclear mechanics polarity

Directional cell migration accompanied by cell polarization is key to the progression of aggressive cancers, such as melanoma (*25*). In cell migration, the nucleus contributes to the establishment of the polarized, directional profile of migrating cells (*26*). It has been found that cell polarization and directional migration require the reorientation of the nucleus, which temporally restricts nuclear rotation that aligns the nuclear major axis with the direction of cell migration (*27*). It has been long hypothesized that the nuclei of polarized cells were also mechanically polarized (*28*, *29*); however, nuclear mechanics in different regions of the nucleus remains unknown because of the lack of tools for performing mechanical measurements on different locations of the cell nuclei in intact cells (*30*).

In our experiments, we introduced a magnetic bead into the cell (bladder cancer cell, T24) through endocytosis (text S4) and controlled its movement from its initial position to a target location on the major axis (Fig. 3C) or minor axis (Fig. 3D) of the cell nucleus. With the GPC controller, we achieved an average position deviation of 0.53 μm from the designed path inside the cell (fig. S4 and movie S3). The slightly larger deviation in the intracellular environment than in cell medium (0.53 μm versus 0.43 μm) may be caused by the complex intracellular environment with cytoskeleton structures and by force disturbances from intracellular force generation motors, such as myosin-II. When the bead reached the target position on the cell nucleus, the system applied a 50-pN force in the direction aligned with the major or minor axis. The applied magnetic forces and nuclear deformations, recorded with an imaging resolution of 200 nm (1 frame/s) and tracking resolution of 0.2 pixel, were fitted into the Hertz model to calculate the apparent Young's modulus, as shown in Fig. 3E. The results (n = 10 cells) summarized in Fig. 3F show that the cell nucleus along its major axis is significantly stiffer than along its minor axis (1.49 ± 0.30 kPa versus 1.07 ± 0.18 kPa; P = 0.0017). Each measurement was repeated three times. We waited (3 min) between each repeated measurement to ensure that the deformation on the cell nucleus fully recovered before the next measurement was made. The sequence of measurements along either major or minor axis was randomly selected via completely randomized design to avoid potential experimental biases between major and minor axes.

The higher apparent Young's modulus along the cell nucleus' major axis demonstrates the polarity of nuclear mechanics under intracellularly applied forces. To understand this polarity, we disrupted the major component of the cytoskeleton actin filaments and microtubules with use of anticytoskeletal drugs. After the cells were treated with the anticytoskeletal drugs, cytochalasin D (CD, which disrupts actin filaments), and nocodazole (NC, which disrupts microtubules), we validated drug effects by staining (Fig. 3, H to J). Nuclear mechanics was then measured along the major and minor axes, and the polarity ratios (defined as the apparent Young's modulus along the major axis over the apparent Young's modulus along the minor axis) for different groups were determined. As shown in Fig. 3G, CD treatment significantly decreased the polarity ratio (control versus CD treated, 1.34 ± 0.19 versus 1.11 ± 0.13; P = 0.008), indicating significant changes of the polarity of nuclear mechanics after actin disruption. As shown in Fig. 3 (H to J) and fig. S6 (A to C), actin filaments largely aligned along the direction of the cell nucleus' major axis in the control group (arrows in the first image of Fig. 3H and fig. S6A), whereas CD treatment largely disrupted the alignment of actin filaments (see the second and fourth images of Fig. 3H and fig. S6A). Because actin filaments are tethered on the cell nucleus and provide tension (*20*), the polarized mechanical properties of the cell nucleus, as revealed by our measurements, are likely attributed to the polarized distribution of actin filaments. After CD treatment, the polarity ratio (1.11 ± 0.13) was marginally larger than one (P = 0.0276). The remaining polarity might be caused by the actin filaments that were not completely disrupted by CD treatment. Although microtubules play a significant role in determining nuclear shape during cell mitosis (*31*, *32*), in the nonmitotic cells measured in our experiments, knocking down microtubules by NC treatment showed no clear change in nuclear size or shape, as shown in Fig. 3J and fig. S7. Our data also showed that the polarity of nuclear mechanics was not altered when microtubules were knocked down (control versus NC treated, 1.34 ± 0.19 versus 1.43 ± 0.18; P = 0.25; Fig. 3G).

Enabled by the 3D manipulation capability of the system, we further conducted cell nucleus polarity measurements in two different Z planes to investigate whether nuclear polarity exists along different heights of the nucleus. As shown in Fig. 4A, we first controlled the

Downloaded from https://www.science.org at The Hong Kong University of Science and Technology (Guangzhou) on May 26, 2026

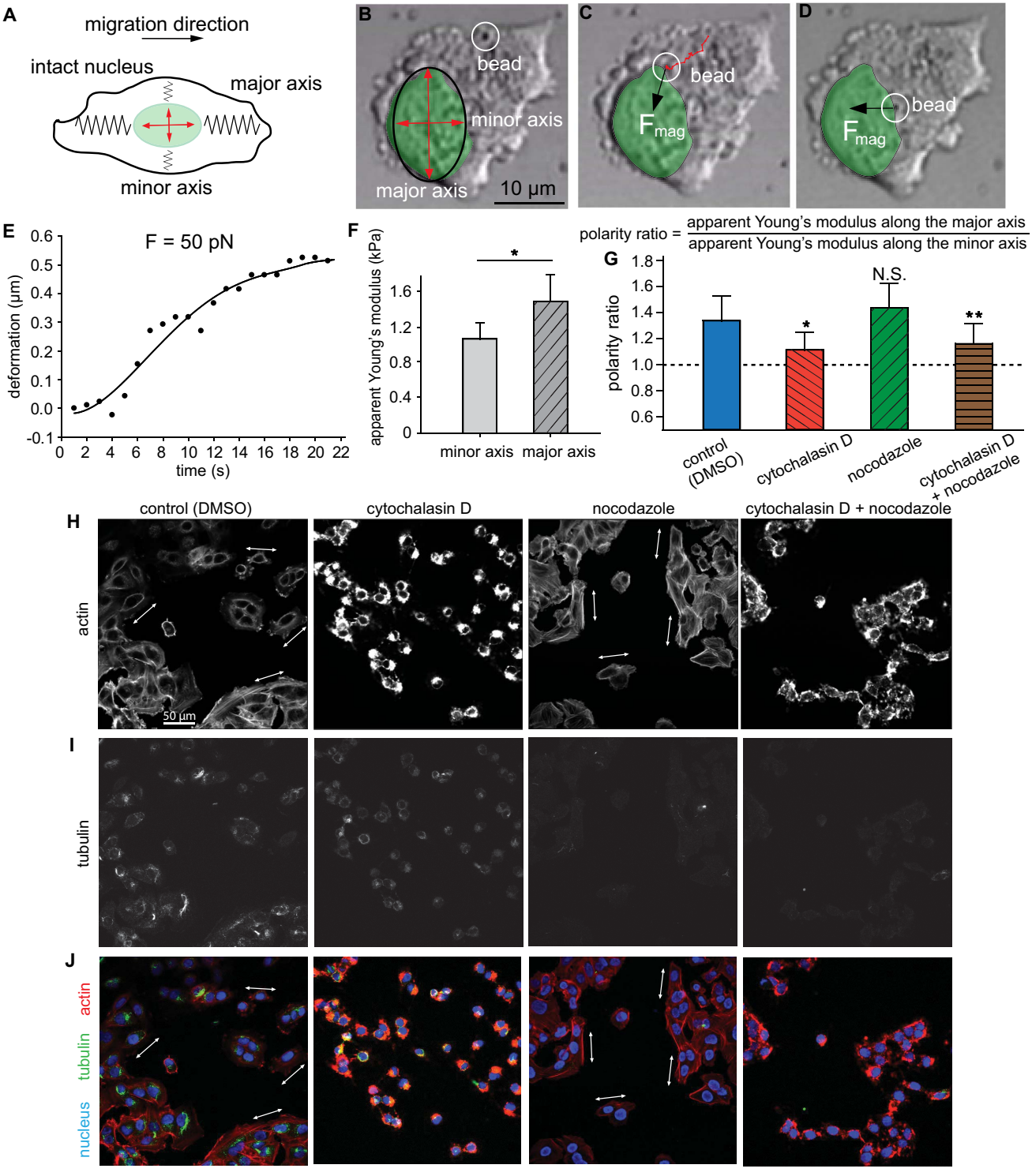

Fig. 3. Spatial measurement of nuclear mechanics polarity. (**A**) Polarity of nuclear mechanics. (**B** to **D**) Magnetic bead introduced into the cell via endocytosis was moved from its initial position to target positions on cell nucleus. The bead's trajectory inside the cell is shown as the red line in (C). (**E**) Experimentally measured nuclear deformation over time. (**F**) Apparent Young's modulus measured from the minor and major axes of the cell nucleus. $n = 10$, error bars: std., $P = 0.0017$. (**G**) Experimentally measured polarity ratio, defined as the apparent Young's modulus measured along the major axis over that measured along the minor axis, of T24 cells. The control group was treated with the drug solvent dimethyl sulfoxide (DMSO). $n = 10$, error bars: std. SD, $^{*}P = 0.008$, $P = 0.25$ (N.S.), $^{**}P = 0.03$. (**H** to **J**) Drug treatment effects in T24 cells. (H) Actin staining showed that the CD treatment disrupted the alignment of actin filaments (second and fourth images). (I) Staining of tubulin, the structural protein of microtubules, showed that microtubules were significantly knocked down after NC treatment (third and fourth images). (J) Costaining of nucleus, actin, and tubulin showed that the major axis of the cell nucleus aligned with actin filaments (first and third images), whereas the CD treatment disrupted the alignment of actin filaments (second and fourth images).

Downloaded from https://www.science.org at The Hong Kong University of Science and Technology (Guangzhou) on May 26, 2026

magnetic bead to navigate onto the nucleus to perform mechanical measurement along the major and minor axes in one focal plane. We then levitated the bead to another focal plane by 0.5 μm to conduct measurements along major and minor axes of the same cell, whose nucleus was about 2 μm in height. The results showed that mechanics polarity exists in both planes, and no significant difference was found between the two *Z* planes measured (polarity ratio in plane 1 versus plane 2, 1.38 ± 0.25 versus 1.34 ± 0.25).

Intracellular temporal measurement of nuclear stiffening

Mechanosensitive stiffening is important for the cell nucleus to withstand forces and protect chromatin from large nuclear deformation, which can induce epigenetic changes (*33*). Recent studies on isolated cell nuclei showed that lamin reinforcement and emerin phosphorylation stiffen the isolated nuclei when subjected to force (*12*). However, the effect of the aggressive nucleus isolation process on nuclear mechanics is unknown, and the cytoskeleton effect was not accounted for because the cytoskeleton was completely removed in the nucleus isolation process.

To understand nuclear stiffening in intact cells, repeated loading needs to be applied on the nuclear envelope inside an intact cell, a task that cannot be achieved by existing techniques. For instance, AFM is only able to apply repeated forces on an isolated nucleus, and single-pole magnetic tweezers are incapable of maintaining the same mechanical load when the bead position changes during measurement. Using the temporal measurement and force control capabilities of our intracellular manipulation and measurement system, we next measured the nuclear mechanics of RT4 cells (early-stage bladder cancer cells) and T24 cells (late-stage bladder cancer cells) multiple times.

In experiments, the bead introduced into a cell through endocytosis was controlled to move from its initial position to a target position on the cell nucleus using GPC position control. When the bead reached the target position, the bead was controlled to apply a 50-pN force on the nucleus in the direction aligned with the major and minor axes (Fig. 5A) for 30 s. The force was then released, and deformation was allowed to recover for 30 s. As shown in Fig. 5B, 30 s for force application and 30 s as the intervals between force applications were sufficient for nuclear deformation to reach equilibrium. After 30-s deformation recovery from the previous loading, the same 50-pN force in the same direction was applied at the same location on the nuclear envelope for 30 s and then released. This process was repeated five times during which the bead positions were recorded with an imaging resolution of 200 nm with a frame rate of 1 frame/s (Fig. 5B).

The magnetic force was maintained as 50 pN during force application through controlling the current in each coil on the basis of the visual feedback of the bead position. The average force error was determined to be 3.29 pN, which was close to the thermal disturbance of 3 pN. The deformation of the cell nucleus decreased from the first measurement to the fifth measurement by about 71% under the same loading of 50 pN, quantitatively describing nucleus stiffening induced by intracellularly applied force in intact cells. We fitted the applied 50-pN magnetic force and the measured nuclear deformation into the standard linear solid viscoelastic model to quantify the effective elastic modulus and viscosity. The results showed that the effective elastic modulus increased with the number of cycles of force application (Fig. 5, D and F), whereas the viscosity value of the cell nuclei remained unchanged (Fig. 5, E and F). Because chromatin inside the cell nucleus largely determines the nucleus' viscosity (*34*, *35*), our data indicate that the occurrence of nuclear stiffening can be independent of chromatin changes.

To understand the role played by major nuclear envelope proteins and cytoskeletal structures in nucleus stiffening, we first knocked down the major nuclear structure protein lamin A/C via small interfering RNA (siRNA) treatment (Fig. 5G) and validated this by Western blot (Fig. 5J). The stiffening ratio, defined as the apparent Young's modulus of the fifth measurement over that of the first measurement, significantly decreased after knocking down lamin A/C (control versus siLamin A/C, 1.17 ± 0.07 versus 1.09 ± 0.05; $P = 0.0007$), indicating less nucleus stiffening. This result supports the potential mechanism that local reinforcement of the lamin A/C filament network underneath the nuclear envelope stiffens the cell nucleus (*12*). Similar to many biopolymer networks, lamin filaments may have reorganized to align with

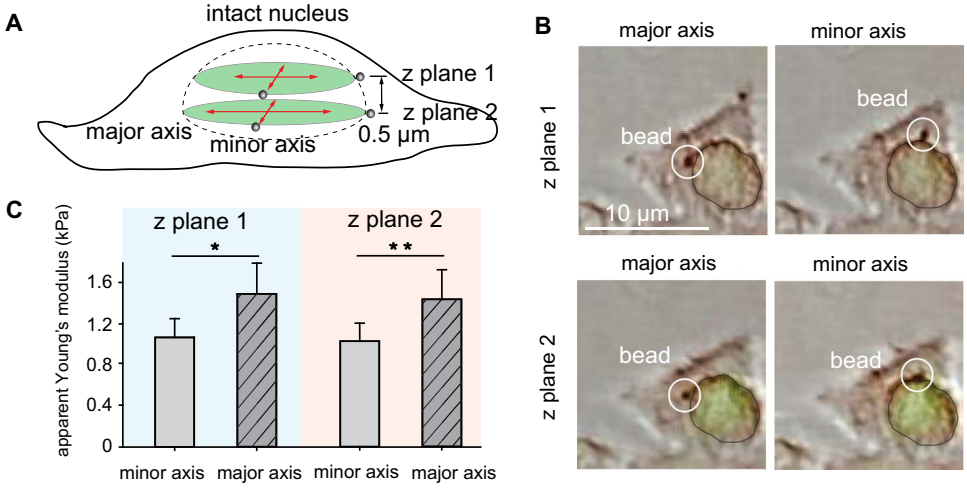

Fig. 4. Nuclear mechanics polarity in different *Z* planes. (**A**) Schematic of nuclear polarity measurement along the major and minor axes of the cell nucleus in two different *Z* planes. (**B**) Representative raw images of nuclear polarity measurement, corresponding to the schematic shown in (A). White circles indicate bead locations. (**C**) The measured apparent Young's modulus results reveal that the major axis is significantly stiffer than the minor axis in both plane 1 and plane 2. $n = 10$ cells, error bar: SDs, $^{*}P < 0.001$, $^{**}P < 0.001$.

Downloaded from https://www.science.org at The Hong Kong University of Science and Technology (Guangzhou) on May 26, 2026

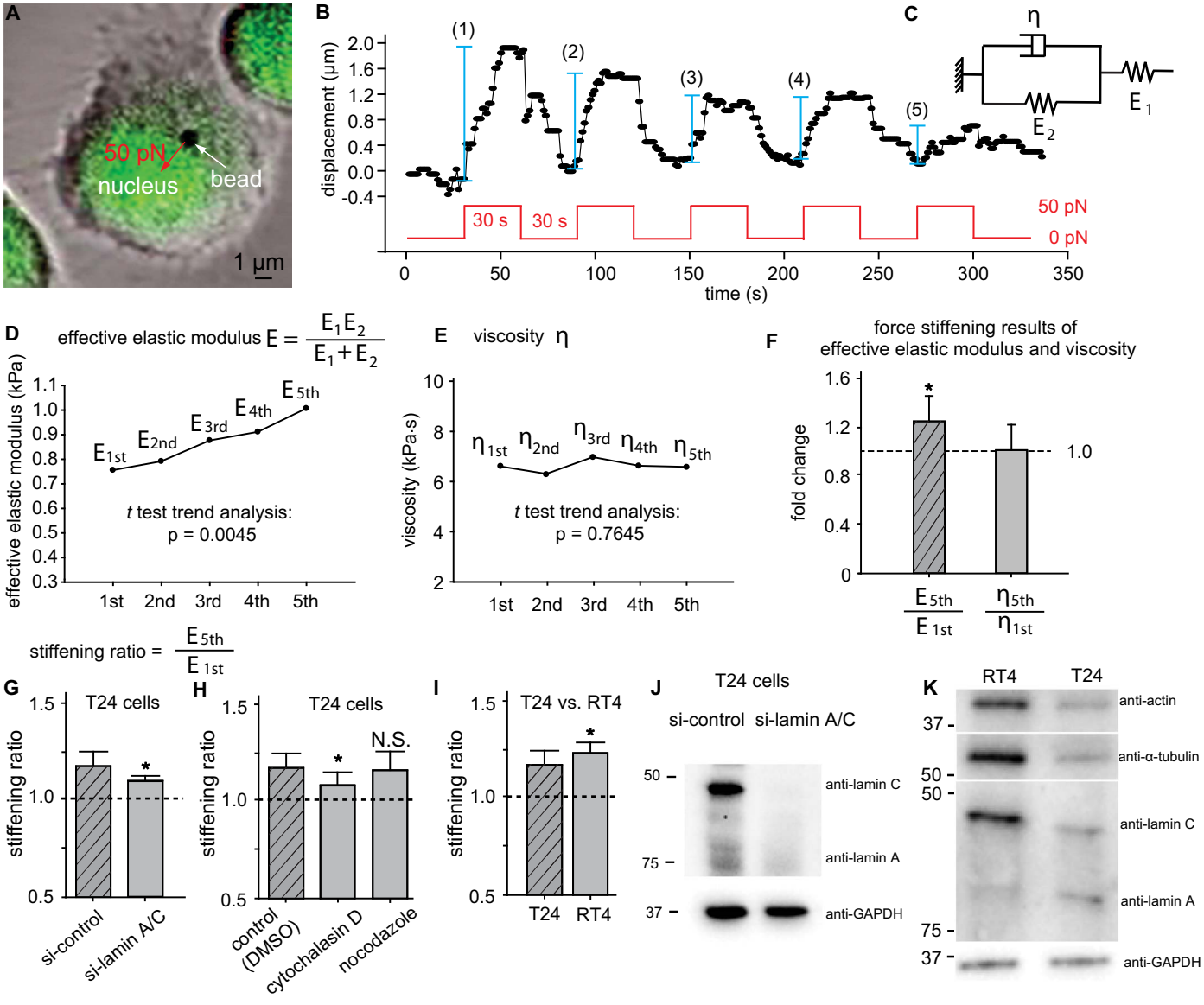

Fig. 5. Temporal measurement of nuclear stiffening. (**A**) The repeated application of 50-pN force on the nuclear envelope while nucleus deformation was recorded over time. (**B**) Magnetic bead displacement during force application and release. The force was applied on the nuclear envelope and released for the nucleus deformation to recover. Repeated loading and recovery was repeated five times in each measurement. Data were interpreted with the standard linear viscoelastic solid model shown in (**C**). (**D** and **E**) Effective elastic modulus and viscosity were quantified for each of the five measurements. (**F**) The fold change of effective elastic modulus and the viscosity after five cycles for force application and release. $n = 10$ cells, error bar: SD. The effective elastic modulus fold change is significantly larger than 1; one-sample t test, $^*P = 0.0003$. The viscosity fold change showed no significant difference compared with 1; one-sample t test, $P = 0.38$. (**G** to **I**) Stiffening ratio is defined as the ratio of effective elastic modulus of the fifth measurement over that of the first measurement. (G) T24 cells after knocking down the nuclear envelope structural protein, lamin A/C via siRNA treatment. $n = 10$, error bar: std., $^*P = 0.0007$. (H) T24 cells after anticytoskeleton drug treatments. $n = 10$, error bar: std., $^*P = 0.0002$, $P = 0.60$ (N.S.). (I) Comparison of stiffening ratio, T24 versus RT4 cells. $n = 10$, error bar: std., $^*P = 0.04$. (**J**) Western blot showing the lamin A/C expression after siRNA treatment, validating the knockdown effect. (**K**) Western blot showing lamin A/C and cytoskeleton differences between RT4 and T24 cells. GAPDH (glyceraldehyde-3-phosphate dehydrogenase) was used as control.

the force application direction for strain stiffening (*36*–*39*). In addition, the cells were treated with anticytoskeleton drugs, CD and NC, to disrupt the major cytoskeletal structures, actin filaments and microtubules, respectively (figs. S6 and S7), and intracellular mechanics measurements were repeated. The results showed that CD treatment induced significant decrease of the stiffening ratio (control versus CD treated, 1.17 ± 0.07 versus 1.08 ± 0.06; $P = 0.0003$; Fig. 5H), whereas no significant decrease of the stiffening ratio occurred after NC treatment. On the basis of the results from lamin A/C knockdown and anticytoskeleton drug treatments, both lamin A/C and actin filaments play important roles in the stiffening of the cell nucleus.

Furthermore, we also measured both early-stage (RT4) and late-stage (T24) human bladder cancer cells by the multipole magnetic tweezers system and compared them with RT4 cells. T24 cells showed a significantly smaller stiffening ratio than RT4 cells (T24 versus RT4, 1.16 ± 0.07 versus 1.22 ± 0.05; $P = 0.04$; Fig. 5F), suggesting less

Downloaded from https://www.science.org at The Hong Kong University of Science and Technology (Guangzhou) on May 26, 2026

stiffening of T24 nuclei than RT4 nuclei. Western blotting revealed significantly less lamin A/C and less actin filaments in T24 than RT4 cells (Fig. 5K), which is consistent with many types of cancer cells that express less lamin A/C and actin as they develop into late stages (*40*, *41*). The lower stiffening effect in T24 nuclei than in RT4 nuclei, which correlates well with the observed lower expression levels of actin filaments and lamin A/C in T24 cells, further supports that the stiffness of the cell nucleus may stem from lamin A/C and actin filaments.

DISCUSSION

The intracellular manipulation system enables submicrometer position control and piconewton force control of a submicrometer magnetic bead inside a single cell. With a generalized predictive controller, the system achieved an average positioning error of 0.4 μm for position control of a 0.7-μm magnetic bead, which enabled the navigation of the submicrometer magnetic bead to different locations inside the cell. The system is capable of exerting forces to the magnetic bead up to 60 pN with a resolution of 4 pN, which was characterized through modeling, simulation, and experimental calibration. Position and force control together enabled spatial and temporal mechanical measurements on the nucleus of an intact cell.

Existing magnetic micromanipulation techniques (*42*) are incapable of efficient 3D control of an object below 1 μm, as required for intracellular measurement, because of poor magnetic force scaling and/or lacking the capability of applying an accurately controlled force. Systems using torque-generated forces would require a long helical tail of over 100 μm to exert a force of tens of piconewtons, making them unsuitable for measurements inside a cell (~20 μm in diameter) (*43*–*45*). Gradient pulling forces can be generated by a number of magnetic field configurations (*46*–*50*). Because the gradient-generated force scales down with the bead size by a factor of 3, the magnetic force exerted on a 1-μm magnetic bead is less than 1 pN (table S3). Conventional magnetic tweezers are single poled. Although they are capable of generating large forces (e.g., tens of piconewtons), the single-axis actuation nature makes the technique incapable of positioning a magnetic bead arbitrarily in the 3D workspace. Compared with other 3D magnetic micromanipulation systems, our new system is capable of generating forces as high as 60 pN on a 0.7-μm bead, navigating the bead to any location inside a cell, and performing intracellular mechanical measurements.

Our experimental results showed that a significantly higher stiffness exists in the cell nucleus' major axis than in the minor axis. In cell migration, actin filaments align with the migration direction (*27*); the aligned actin filaments may provide stronger tethering in the major axis of the nucleus for restricting the rotation of the cell nucleus (*51*). The stronger tethering in the aligned direction of actin filaments potentially explains the polarity of the nuclear mechanics, which was significantly disrupted after actin filaments were knocked down. Our results also revealed that an intracellularly applied force induced the stiffening of the cell nucleus. The elastic modulus and the viscosity of the cell nucleus measured using the multipole magnetic tweezers are in agreement with previously reported values (*12*, *34*, *52*). The force applied on the cell nucleus could trigger epigenetic changes within the nucleus, including changes in chromatin structures, protein-chromatin bindings, and transcription factor bindings (*53*). Compared with the early-stage human bladder cancer cells RT4, the late-stage T24 cells exhibited significantly less stiffening upon force application on the nucleus, indicating that T24 cells would have larger nuclear deformation when subjected to repeated mechanical stimulation, which cancer cells experience during metastasis when they travel through confined spaces (*54*, *55*). Larger nuclear deformation could potentially induce gene mutations to facilitate metastasis (*56*).

The creep response of isolated cell nuclei showed that the isolated nucleus stiffens under force application (*12*). Isolated nuclei and nuclei in intact cells are known to exhibit distinct mechanical properties; i.e., the isolated nucleus has lower elastic modulus and lower viscosity than the intact nucleus of the same cell type (*57*–*59*). The tethering from the cytoskeleton onto the nuclear envelope increases the elastic modulus by providing mechanical support to the cell nucleus and increases the viscosity of the nucleus by providing cushion effects to the cell nucleus when subjected to an extracellular force (*59*). Besides the loss of the cytoskeleton, isolating the cell nucleus also disturbs the normal lamin architecture and the chemical compositions of nucleoplasm and cytoplasm (*60*, *61*). Although the cytoskeleton effect was lacking in the stiffening of isolated nuclei reported in (*12*), our experiments were performed on nucleus in intact cells and revealed the cytoskeleton effect on nucleus stiffening (Fig. 5H). Knocking down actin through CD treatment, the stiffening ratio decreased by about 10% (control versus CD treated, 1.17 ± 0.07 versus 1.08 ± 0.06; $P = 0.0003$), but no significant decrease of the stiffening ratio occurred after knocking down microtubules through NC treatment.

Our system enables both spatial and temporal intracellular measurement, providing a powerful platform technology for single-cell analysis. It permits cell mechanics and mechanotransduction to be studied at different locations inside an intact cell and at different time points during a cellular process (e.g., migration and mitosis). The capability of applying precise intracellular forces circumvents the cytoskeleton and directly exerts forces on the cell nucleus. Besides biophysical measurement, the submicrometer magnetic bead can also be chemically functionalized (e.g., with pH-sensitive or Ca^{2+}-sensitive fluorophores) for intracellular biochemical sensing (*62*, *63*).

In our system, the close distance between magnetic poles was necessary for generating a force as large as 60 pN on a submicrometer magnetic bead, which also results in a small workspace. The small workspace limits the number of the cells to be imaged and measured. To overcome this limitation, we designed the device with a top stage and a bottom stage, between which a coverslip cultured with cells can be moved freely to bring more cells into the workspace of the device and the field of view of the microscope for measurement. The close distance between poles also poses challenges for accurate alignment of the poles. Unbalanced pole pairs would drag the magnetic bead toward the stronger pole, which could further limit the size of the workspace. In our design, adjustments were made with ultrafine adjustment screws and micromanipulators, and the magnetic poles were assembled/aligned with an accuracy better than 1 μm. This accuracy can be further improved by directly forming magnetic poles via sputtering and microfabrication.

The system's positioning capability is limited by the imaging resolution and sampling frequency of the laser scanning confocal microscopy. The multipole magnetic tweezers device could be integrated with more advanced imaging techniques, such as super-resolution structured illumination microscopy (*64*) for better imaging resolution (e.g., from 200 to 120 nm) and a higher sampling frequency (e.g., from 1 to 4 to 30 Hz). In addition, for tasks that require the targeting of a specific protein [typically <20 nm (*65*), such as Nesprin], visual servo position control could readily navigate a submicrometer magnetic

Downloaded from https://www.science.org at The Hong Kong University of Science and Technology (Guangzhou) on May 26, 2026

bead to the vicinity of the target, and then protein-protein interactions between the antibody coated on the magnetic bead (e.g., anti-Nesprin antibody) and the target protein (Nesprin) could bind the bead accurately to the target protein, beyond the limit imposed by the 120-nm imaging resolution.

MATERIALS AND METHODS

Study design and statistical analysis

The experiments (Figs. 3 to 5) were designed to prove the polarity of nuclear mechanics and the stiffening of the cell nucleus. The sample size was chosen larger than 10 cells to cover the variance among the cells. Drug treatment, immunofluorescent staining, siRNA treatment, and Western blot are detailed in the Supplementary Materials (text S4). The staining and Western blot were replicated three times.

The polarity ratio and the stiffening ratio were reported as means ± SD. Comparisons of each group were conducted by one-way analysis of variance (ANOVA) and Student-Newman-Keuls test for pairwise comparisons in JMP. The statistical significance in each comparison was evaluated as $P < 0.05$ for significance level.

Device fabrication and assembly

The 3D magnetic tweezers consist of six magnetic poles with sharp tips (three poles placed in one plane and the other three poles placed in a different plane), a magnetic yoke, and coils. To achieve a large magnetic field gradient, we made the magnetic poles of high-permeability foils (Silicon Iron, MuShield) and fabricated the tips by electric discharge machining (Sodick AD325L CNC Wire EDM; tolerance, ±5 μm). The magnetic yoke were fabricated through CNC machining with a tolerance of ±0.1 mm. Coils (Magnetic Wire, gauge 14, Digi-Key) were wired onto the cores on the yoke. The magnetic poles were assembled onto acrylic plate with alignment marks engraved by laser machining under a microscope to ensure the alignment of each pole pairs within the same stage (either top stage or bottom stage). After assembling the top stage and bottom stage separately, we adjusted the alignment between the top and bottom stages by tuning the upright ultrafine adjustment screw on the top stage for Z-axis alignment and by tuning the two other ultrafine adjustment screws on the side of the top stage for X-Y alignment. Three linear shafts and three linear ball bearings were integrated to ensure that the top stage and the bottom stage were parallel to each other. The temperatures on the magnetic coil, magnetic pole, and workspace were measured in the highest current setting during 5-min experiments (longest duration for measuring nucleus stiffening). The coil temperature increased from a room temperature of 22.6° to 26.9°C, the pole tip temperature slightly changed from 22.7° to 24.7°C, and the workspace temperature increase was negligible, from 22.6° to 22.8°C.

Viscoelastic model

The standard linear viscoelastic model is commonly used for describing viscoelastic properties of cellular structures because it describes both time-variant (the dashpot) and time-invariant (the spring) relationships between stress and strain (*12*, *57*). For a viscoelastic material like the cell nucleus, the compliance in the standard linear solid model is

$$J(t) = \frac{\varepsilon}{\sigma} = \frac{1}{E_1} + \frac{1}{E_2}\left(1 - e^{-\frac{t}{\tau}}\right) \quad (6)$$

where σ is stress, ε is strain, $\tau = \eta/E_2$ is the viscosity of the sample, η is the viscosity, and the effective elastic modulus equals $\frac{E_1E_2}{E_1+E_2}$.The displacement of the bead is

$$\text{displacement}(t) = \frac{1}{6\pi r} J(t) F \quad (7)$$

where r is the radius of the magnetic bead (r = 0.35 μm) and F is the force applied in experiments (F = 50 pN).

According to the standard linear solid viscoelastic model, viscoelastic deformation recovers with strain after an exponential decay (*66*). On the basis of the measured viscoelastic properties, the elastic modulus was 0.76 to 0.93 kPa, and the viscosity was 6.31 to 6.98 kPa·s, indicating a time constant of ~8 s, which is in agreement with previous work on the viscoelastic properties of the cell nucleus (*52*, *59*). Measurement during the recovery of the cell nucleus leads to hysteresis of the viscoelastic material and results in a higher effective elastic modulus value. In this work, we waited for sufficiently long (3 min, compared with 8 s of time constant) between each repeated measurement to avoid hysteresis caused by viscoelastic deformation.

SUPPLEMENTARY MATERIALS

robotics.sciencemag.org/cgi/content/full/4/28/eaav6180/DC1
Text S1. Calculation of the force required for intracellular measurements
Text S2. Magnetic bead position control
Text S3. Nuclear deformation under different image capturing rates
Text S4. Supplementary methods and materials
Fig. S1. Cell viability test and success rate of cell endocytosis.
Fig. S2. Generalized predictive control.
Fig. S3. Trajectory tracking performance using PID and GPC.
Fig. S4. Intracellular navigation performance.
Fig. S5. Viscoelastic parameters of major and minor axes of T24 cells.
Fig. S6. Staining of actin and tubulin for single T24 cells.
Fig. S7. Staining of actin and tubulin for validation of the drug treatment effects in RT4 cells.
Fig. S8. Nuclear deformation under different image capturing frame rates.
Fig. S9. Top down and side view of the device and scanning electron microscope images of the microbead and pole tip.
Fig. S10. Mean square displacement over lag time for bead position tracking.
Table S1. Key parameters in system design.
Table S2. Key parameters in the generalized predictive controller.
Table S3. Representative 3D magnetic micromanipulation systems.
Movie S1. System design.
Movie S2. Position control of magnetic bead.
Movie S3. Intracellular navigation and nuclear polarity measurement.
Movie S4. Intracellular force application on cell nucleus for stiffening measurement.
Movie S5. Simultaneous bright-field and fluorescence imaging.
Movie S6. Raw video of nuclear deformation and recovery after 50-pN force application.
Movie S7. Raw video of multibead navigating inside the silicone oil in calibration experiments.
References (*67*–*74*)

REFERENCES AND NOTES

1. J. Liu, J. Wen, Z. Zhang, H. Liu, Y. Sun, Voyage inside the cell: Microsystems and nanoengineering for intracellular measurement and manipulation. *Microsyst. Nanoeng.* **1**, 15020 (2015).
2. M. Zwerger, C. Y. Ho, J. Lammerding, Nuclear mechanics in disease. *Annu. Rev. Biomed. Eng.* **13**, 397–428 (2011).
3. H. Liu, J. Wen, Y. Xiao, J. Liu, S. Hopyan, M. Radisic, C. A. Simmons, Y. Sun, In situ mechanical characterization of the cell nucleus by atomic force microscopy. *ACS Nano* **8**, 3821–3828 (2014).
4. D. A. Fletcher, R. D. Mullins, Cell mechanics and the cytoskeleton. *Nature* **463**, 485–492 (2010).
5. A. K. M. Lam, A. Galione, The endoplasmic reticulum and junctional membrane communication during calcium signaling. *Biochim. Biophys. Acta* **1833**, 2542–2559 (2013).
6. J. Liu, Z. Zhang, H. Tao, J. Ge, H. Liu, J. Wen, S. Hopyan, H. Pu, S. Xie, Y. Sun, Robotic fluidic jet for automated cellular and intracellular mechanical characterization, in

Downloaded from https://www.science.org at The Hong Kong University of Science and Technology (Guangzhou) on May 26, 2026

IEEE International Conference on Information and Automation (ICIA'16) (IEEE, 2016), pp. 462–467.
7. K. Mandal, A. Asnacios, B. Goud, J.-B. Manneville, Mapping intracellular mechanics on micropatterned substrates. *Proc. Natl. Acad. Sci. U.S.A.* **113**, E7159–E7168 (2016).
8. W. Wang, S. Li, L. Mair, S. Ahmed, T. J. Huang, T. E. Mallouk, Acoustic propulsion of nanorod motors inside living cells. *Angew. Chem. Int. Ed.* **53**, 3201–3204 (2014).
9. M. Pal, N. Somalwar, A. Singh, R. Bhat, S. M. Eswarappa, D. K. Saini, Maneuverability of magnetic nanomotors inside living cells. *Adv. Mater.* **30**, 1800429 (2018).
10. O. Felfoul, M. Mohammadi, S. Taherkhani, D. de Lanauze, Y. Z. Xu, D. Loghin, S. Essa, S. Jancik, D. Houle, M. Lafleur, L. Gaboury, M. Tabrizian, N. Kaou, M. Atkin, T. Vuong, G. Batist, N. Beauchemin, D. Radzioch, S. Martel, Magneto-aerotactic bacteria deliver drug-containing nanoliposomes to tumour hypoxic regions. *Nat. Nanotechnol.* **11**, 941–947 (2016).
11. E. Diller, M. Sitti, Three-dimensional programmable assembly by untethered magnetic robotic micro-grippers. *Adv. Funct. Mater.* **24**, 4397–4404 (2014).
12. C. Guilluy, L. D. Osborne, L. Van Landeghem, L. Sharek, R. Superfine, R. Garcia-Mata, K. Burridge, Isolated nuclei adapt to force and reveal a mechanotransduction pathway in the nucleus. *Nat. Cell Biol.* **16**, 376–381 (2014).
13. M. P. Kummer, J. J. Abbott, B. E. Kratochvil, R. Borer, A. Sengul, B. J. Nelson, OctoMag: An electromagnetic system for 5-DOF wireless micromanipulation. *IEEE Trans. Robot.* **26**, 1006–1017 (2010).
14. D. Son, M. D. Dogan, M. Sitti, Magnetically actuated soft capsule endoscope for fine-needle aspiration biopsy, in *IEEE International Conference on Robotics and Automation (ICRA'17)* (IEEE, 2017), pp. 1132–1139.
15. M. S. Sakar, E. B. Steager, A. Cowley, V. Kumar, G. J. Pappas, Wireless manipulation of single cells using magnetic microtransporters, in *IEEE International Conference on Robotics and Automation (ICRA'11)* (IEEE, 2011), pp. 2668–2673.
16. I. S. M. Khalil, D. Mahdy, A. El Sharkawy, R. R. Moustafa, A. F. Tabak, M. E. Mitwally, S. Hesham, N. Hamdi, A. Klingner, A. Mohamed, M. Sitti, Mechanical rubbing of blood clots using helical robots under ultrasound guidance. *IEEE Robot. Autom. Lett.* **3**, 1112–1119 (2018).
17. A. Hosney, J. Abdalla, I. S. Amin, N. Hamdi, I. S. Khalil, In vitro validation of clearing clogged vessels using microrobots, in *6th IEEE International Conference on Biomedical Robotics and Biomechatronics (BioRob'16)* (IEEE, 2016), pp. 272–277.
18. X. Wang, M. Luo, H. Wu, Z. Zhang, J. Liu, Z. Xu, W. Johnson, Y. Sun, A three-dimensional magnetic tweezer system for intraembryonic navigation and measurement. *IEEE Trans. Robot.* **34**, 240–247 (2018).
19. J. J. Abbott, K. E. Peyer, L. X. Dong, B. J. Nelson, How should microrobots swim? *Int. J. Rob. Res.* **66**, 157–167 (2010).
20. A. H. B. de Vries, B. E. Krenn, R. van Driel, J. S. Kanger, Micro magnetic tweezers for nanomanipulation inside live cells. *Biophys. J.* **88**, 2137–2144 (2005).
21. J. K. Fisher, J. Cribb, K. V. Desai, L. Vicci, B. Wilde, K. Keller, R. M. Taylor II, J. Haase, K. Bloom, E. T. O'Brien, R. Superfine, Thin-foil magnetic force system for high-numerical-aperture microscopy. *Rev. Sci. Instrum.* **77**, nihms8302 (2006).
22. Z. Zhang, K. Huang, C.-H. Menq, Design, implementation, and force modeling of quadrupole magnetic tweezers. *IEEE ASME Trans. Mechatron.* **15**, 704–713 (2010).
23. M. Kharboutly, M. Gauthier, N. Chaillet, Predictive control of a micro bead's trajectory in a dielectrophoresis-based device, in *IEEE/RSJ International Conference on Intelligent Robots and Systems (IROS'10)* (IEEE, 2010), pp. 5616–5621.
24. S. Chidrawar, B. Patre, Generalized predictive control and neural generalized predictive control. *Leonardo J. Sci.* **7**, 133–152 (2008).
25. J. Park, W. R. Holmes, S. H. Lee, H.-N. Kim, D.-H. Kim, M. K. Kwak, C. J. Wang, L. Edelstein-Keshet, A. Levchenko, Mechanochemical feedback underlies coexistence of qualitatively distinct cell polarity patterns within diverse cell populations. *Proc. Natl. Acad. Sci. U.S.A.* **114**, E5750–E5759 (2017).
26. M. Maninová, Z. Klímová, J. T. Parsons, M. J. Weber, M. P. Iwanicki, T. Vomastek, The reorientation of cell nucleus promotes the establishment of front–rear polarity in migrating fibroblasts. *J. Mol. Biol.* **425**, 2039–2055 (2013).
27. M. Maninová, M. P. Iwanicki, T. Vomastek, Emerging role for nuclear rotation and orientation in cell migration. *Cell Adh. Migr.* **8**, 42–48 (2014).
28. M. Versaevel, T. Grevesse, S. Gabriele, Spatial coordination between cell and nuclear shape within micropatterned endothelial cells. *Nat. Commun.* **3**, 671 (2012).
29. B. Chen, G. Kumar, C. C. Co, C.-C. Ho, Geometric control of cell migration. *Sci. Rep.* **3**, 2827 (2013).
30. J. Lammerding, K. N. Dahl, D. E. Discher, R. D. Kamm, Nuclear mechanics and methods. *Methods Cell Biol.* **83**, 269–294 (2007).
31. J. Z. Xue, H. Funabiki, Nuclear assembly shaped by microtubule dynamics. *Nucleus* **5**, 40–46 (2014).
32. M. Webster, K. L. Witkin, O. Cohen-Fix, Sizing up the nucleus: Nuclear shape, size and nuclear-envelope assembly. *J. Cell Sci.* **122**, 1477–1486 (2009).
33. R. P. Martins, J. D. Finan, G. Farshid, D. A. Lee, Mechanical regulation of nuclear structure and function. *Annu. Rev. Biomed. Eng.* **14**, 431–455 (2012).
34. S. M. Schreiner, P. K. Koo, Y. Zhao, S. G. J. Mochrie, M. C. King, The tethering of chromatin to the nuclear envelope supports nuclear mechanics. *Nat. Commun.* **6**, 7159 (2015).
35. S. D. Thorpe, D. A. Lee, Dynamic regulation of nuclear architecture and mechanics—A rheostatic role for the nucleus in tailoring cellular mechanosensitivity. *Nucleus* **8**, 287–300 (2017).
36. A. Banerjee, V. Rathee, R. Krishnaswamy, P. Bhattacharjee, P. Ray, A. K. Sood, K. Sengupta, Viscoelastic behavior of human lamin A proteins in the context of dilated cardiomyopathy. *PLOS ONE* **8**, e83410 (2013).
37. G. Žagar, P. R. Onck, E. van der Giessen, Two fundamental mechanisms govern the stiffening of cross-linked networks. *Biophys. J.* **108**, 1470–1479 (2015).
38. A. D. Stephens, E. J. Banigan, S. A. Adam, R. D. Goldman, J. F. Marko, Chromatin and lamin A determine two different mechanical response regimes of the cell nucleus. *Mol. Biol. Cell* **28**, 1984–1996 (2017).
39. J. Xu, Y. Tseng, D. Wirtz, Strain hardening of actin filament networks. Regulation by the dynamic cross-linking protein α-actinin. *J. Biol. Chem.* **275**, 35886–35892 (2000).
40. K. M. Sakthivel, P. Sehgal, A novel role of lamins from genetic disease to cancer biomarkers. *Oncol. Rev.* **10**, 309 (2016).
41. P. M. Davidson, J. Lammerding, Broken nuclei–lamins, nuclear mechanics, and disease. *Trends Cell Biol.* **24**, 247–256 (2014).
42. E. Diller, M. Sitti, Untethered magnetic micromanipulation, in *Micro-and Nanomanipulation Tools* (Wiley-VCH Verlag GmbH, 2015), pp. 259–282.
43. K. E. Peyer, L. Zhang, B. J. Nelson, Bio-inspired magnetic swimming microrobots for biomedical applications. *Nanoscale* **5**, 1259–1272 (2013).
44. S. Tottori, L. Zhang, F. Qiu, K. K. Krawczyk, A. Franco-Obregón, B. J. Nelson, Magnetic helical micromachines: Fabrication, controlled swimming, and cargo transport. *Adv. Mater.* **24**, 811–816 (2012).
45. L. Zhang, J. J. Abbott, L. Dong, K. E. Peyer, B. E. Kratochvil, H. Zhang, C. Bergeles, B. J. Nelson, Characterizing the swimming properties of artificial bacterial flagella. *Nano Lett.* **9**, 3663–3667 (2009).
46. I. S. M. Khalil, V. Magdanz, S. Sanchez, O. G. Schmidt, S. Misra, Precise localization and control of catalytic Janus micromotors using weak magnetic fields. *Int. J. Adv. Robot. Syst.* **12**, 1 (2015).
47. Z. Zhang, C.-H. Menq, Three-dimensional particle tracking with subnanometer resolution using off-focus images. *Appl. Optics* **47**, 2361–2370 (2008).
48. P. Ryan, E. Diller, Magnetic actuation for full dexterity microrobotic control using rotating permanent magnets. *IEEE Trans. Robot.* **33**, 1398–1409 (2017).
49. M. Vonthron, V. Lalande, G. Bringout, C. Tremblay, S. Martel, A MRI-based integrated platform for the navigation of micro-devices and microrobots, in *IEEE/RSJ International Conference on Intelligent Robots and Systems (IROS'11)* (IEEE, 2011), pp. 1285–1290.
50. X. Wang, Z. Zhang, H. Tao, J. Liu, S. Hopyan, Y. Sun, Characterizing inner pressure and stiffness of trophoblast and inner cell mass of blastocysts. *Biophys. J.* **12**, 2443–2450 (2018).
51. M. C. Keeling, L. R. Flores, A. H. Dodhy, E. R. Murray, N. Gavara, Actomyosin and vimentin cytoskeletal networks regulate nuclear shape, mechanics and chromatin organization. *Sci. Rep.* **7**, 5219 (2017).
52. F. Guilak, J. R. Tedrow, R. Burgkart, Viscoelastic properties of the cell nucleus. *Biochem. Biophys. Res. Commun.* **269**, 781–786 (2000).
53. C. M. Denais, R. M. Gilbert, P. Isermann, A. L. McGregor, M. te Lindert, B. Weigelin, P. M. Davidson, P. Friedl, K. Wolf, J. Lammerding, Nuclear envelope rupture and repair during cancer cell migration. *Science* **352**, 353–358 (2016).
54. M. Raab, M. Gentili, H. de Belly, H.-R. Thiam, P. Vargas, A. J. Jimenez, F. Lautenschlaeger, R. Voituriez, A.-M. Lennon-Duménil, N. Manel, M. Piel, ESCRT III repairs nuclear envelope ruptures during cell migration to limit DNA damage and cell death. *Science* **352**, 359–362 (2016).
55. J. Irianto, Y. Xia, C. R. Pfeifer, A. Athirasala, J. Ji, C. Alvey, M. Tewari, R. R. Bennett, S. M. Harding, A. J. Liu, R. A. Greenberg, D. E. Discher, DNA damage follows repair factor depletion and portends genome variation in cancer cells after pore migration. *Curr. Biol.* **27**, 210–223 (2017).
56. R. A. Burrell, N. McGranahan, J. Bartek, C. Swanton, The causes and consequences of genetic heterogeneity in cancer evolution. *Nature* **501**, 338–345 (2013).
57. A. C. Rowat, J. Lammerding, J. H. Ipsen, Mechanical properties of the cell nucleus and the effect of emerin deficiency. *Biophys. J.* **91**, 4649–4664 (2006).
58. K. Haase, J. K. L. Macadangdang, C. H. Edrington, C. M. Cuerrier, S. Hadjiantoniou, J. L. Harden, I. S. Skerjanc, A. E. Pelling, Extracellular forces cause the nucleus to deform in a highly controlled anisotropic manner. *Sci. Rep.* **6**, 21300 (2016).
59. X. Wang, H. Liu, M. Zhu, C. Cao, Z. Xu, Y. Tsatskis, K. Lau, C. Kuok, T. Filleter, H. McNeill, C. A. Simmons, S. Hopyan, Y. Sun, Mechanical stability of the cell nucleus: Roles played by the cytoskeleton in nuclear deformation and strain recovery. *J. Cell Sci.* **131**, jcs209627 (2018).
60. J. Lammerding, Mechanics of the nucleus. *Compr. Physiol.* **1**, 783–807 (2011).
61. K. N. Dahl, A. J. Engler, J. D. Pajerowski, D. E. Discher, Power-law rheology of isolated nuclei with deformation mapping of nuclear substructures. *Biophys. J.* **89**, 2855–2864 (2005).

Downloaded from https://www.science.org at The Hong Kong University of Science and Technology (Guangzhou) on May 26, 2026

62. J. V. Jokerst, Z. Chen, L. Xu, R. Nolley, E. Chang, B. Mitchell, J. D. Brooks, S. S. Gambhir, A magnetic bead-based sensor for the quantification of multiple prostate cancer biomarkers. *PLOS ONE* **10**, e0139484 (2015).
63. H. Liu, H. Maruyama, T. Masuda, A. Honda, F. Arai, Multi-fluorescent micro-sensor for accurate measurement of pH and temperature variations in micro-environments. *Sens. Actuators, B* **203**, 54–62 (2014).
64. R. Heintzmann, T. Huser, Super-resolution structured illumination microscopy. *Chem. Rev.* **117**, 13890–13898 (2017).
65. Harvard, Key numbers for cell biologists (BioNumbers, 2014); http://bionumbers.hms.harvard.edu/KeyNumbers.aspx.
66. D. Roylance, "Engineering viscoelasticity" (Massachusetts Institute of Technology Cambridge, 2001); http://web.mit.edu/course/3/3.11/www/modules/visco.pdf.
67. D. Jia, J. Hamilton, L. M. Zaman, A. Goonewardene, The time, size, viscosity, and temperature dependence of the Brownian motion of polystyrene microspheres. *Am. J. Phys.* **75**, 111–115 (2007).
68. M. Doi, *Soft Matter Physics* (Oxford Univ. Press, 2013).
69. M. P. Marder, *Condensed Matter Physics* (John Wiley & Sons, 2010).
70. P. K. Karkoulis, D. J. Stravopodis, L. H. Margaritis, G. E. Voutsinas, 17-Allylamino-17-demethoxygeldanamycin induces downregulation of critical Hsp90 protein clients and results in cell cycle arrest and apoptosis of human urinary bladder cancer cells. *BMC Cancer* **10**, 481 (2010).
71. S. W. Hell, Far-field optical nanoscopy. *Science* **316**, 1153–1158 (2007).
72. B. Huang, H. Babcock, X. Zhuang, Breaking the diffraction barrier: Super-resolution imaging of cells. *Cell* **143**, 1047–1058 (2010).
73. J. Liu, V. Siragam, Z. Gong, J. Chen, M. D. Fridman, C. Leung, Z. Lu, C. Ru, S. Xie, J. Luo, R. M. Hamilton, Y. Sun, Robotic adherent cell injection for characterizing cell–cell communication. *IEEE Trans. Biomed. Eng.* **62**, 119–125 (2015).
74. S. Schuerle, S. Erni, M. Flink, B. E. Kratochvil, B. J. Nelson, Three-dimensional magnetic manipulation of micro- and nanostructures for applications in life sciences. *IEEE Trans. Magn.* **49**, 321–330 (2013).

Acknowledgments: We thank J. Liu and X. Huang for helpful suggestions. **Funding:** This work was supported by the National Sciences and Engineering Research Council of Canada and the Canadian Institutes of Health Research via an NSERC Discovery Grant and a Collaborative Health Research Projects (CHRP) Grant, by the Ontario Research Fund via the Research Excellence Program, by the Canada Research Chairs program, and by the Canadian Institutes of Health Research (143319 to H.M.). H.M. was also supported by the BJC investigator program. **Author contributions:** X.W., F.W., M.T., S.H., H.M., and Y.S. designed the study. X.W., C.H., Y.T., J.L., Z.Z., M.Z., and C.D. performed experiments. H.M. and Y.S. provided the funding. X.W., Y.T., S.H., H.M., and Y.S. wrote the paper. **Competing interests:** The authors declare that they have no competing interests. **Data and materials availability:** All data needed to evaluate the conclusions in the paper are present in the paper or the Supplementary Materials. The data and the code for this study have been deposited in GitHub at https://github.com/XianShawn/intracellular-magnetic-tweezers.

Submitted 3 October 2018
Accepted 16 January 2019
Published 13 March 2019
10.1126/scirobotics.aav6180

Citation: X. Wang, C. Ho, Y. Tsatskis, J. Law, Z. Zhang, M. Zhu, C. Dai, F. Wang, M. Tan, S. Hopyan, H. McNeill, Y. Sun, Intracellular manipulation and measurement with multipole magnetic tweezers. *Sci. Robot.* **4**, eaav6180 (2019).

Downloaded from https://www.science.org at The Hong Kong University of Science and Technology (Guangzhou) on May 26, 2026

Science Robotics

Intracellular manipulation and measurement with multipole magnetic tweezers

X. Wang, C. Ho, Y. Tsatskis, J. Law, Z. Zhang, M. Zhu, C. Dai, F. Wang, M. Tan, S. Hopyan, H. McNeill, and Y. Sun

Sci. Robot. **4** (28), eaav6180. DOI: 10.1126/scirobotics.aav6180

View the article online
https://www.science.org/doi/10.1126/scirobotics.aav6180
Permissions
https://www.science.org/help/reprints-and-permissions

Downloaded from https://www.science.org at The Hong Kong University of Science and Technology (Guangzhou) on May 26, 2026

Use of this article is subject to the Terms of service

Science Robotics (ISSN 2470-9476) is published by the American Association for the Advancement of Science. 1200 New York Avenue NW, Washington, DC 20005. The title *Science Robotics* is a registered trademark of AAAS.

Copyright © 2019 The Authors, some rights reserved; exclusive licensee American Association for the Advancement of Science. No claim to original U.S. Government Works